NUMERICAL SIMULATION OF GAS-SOLID HEAT TRANSFER AND MOISTURE EVAPORATION PROCESS IN PREHEATING SHAFT KILN FOR FERROMAGNESIUM PELLETS

Shaopei DUAN [*], *Ning DING, Shuo WANG, Baokuan LI*

School of Metallurgy, Northeastern University, Shenyang 110819, China

[*] Corresponding author; E-mail: duanshaopei_neu@163.com

The arc furnace is an important equipment in the production of manganese ferroalloys. In the smelting process, it produces high temperature flue gas above 700 K, which has high utilization value. During the pelleting process, moisture exists on the surface and inside of the pellets, which, if directly fed into the arc furnace, will lower the temperature of the furnace, affecting the production, and will also cause the pellets to burst, resulting in pressure fluctuations in the furnace and other hazards. The preheating shaft kiln reduces the moisture content of the pellet while preheating the pellet by utilizing high temperature flue gas. In this paper, through the establishment of porous media and shrinking core coupling mathematical model, to achieve the prediction of the heating and drying process of the pellets of various particle sizes, which is in good agreement with the production monitoring data. The results show that 9~11 mm pellets have the best preheating effect in terms of tail gas temperature, pellet temperature and preheating time.

Key words*: preheating shaft kiln, ferromanganese pellets, gas-solid heat transfer, moisture evaporation, numerical simulation*

1. Introduction

Manganese has a wide range of uses, with 90% to 95% of manganese being used in the metallurgical industry, as well as in batteries, ceramics and chemistry [1]. In the metallurgical industry, manganese alloys are an ideal deoxidizer and desulfurizer, and are widely used in the production of mild and stainless steels, which is very important role and position in the steel industry [2].

The arc furnace method is the most commonly used method to produce manganese alloys in industry [3,4,5], and the total amount of manganese ferroalloys smelted using the arc furnace accounts for about 80% of the total production. The arc furnace is a high-energy consuming equipment. Therefore, the high-temperature flue gas produced by the smelting process has a high utilization value.

In 1990, the Metso's Outotec installed a shaft kiln for preheating chrome pellets on top of the arc furnace [6], which directly realizes the preheating of ferrochrome pellets. In recent years, companies have introduced this preheating technology, which makes the electricity consumption per ton of product reduced to 2708 kW-h, the design cost of this new type of preheating kiln accounted for less than 1% of the total cost.

After pelleting and cleaning of ferromanganese pellets, the surface and the inside of the pellet are wet, and the wet pellet is prone to bursting phenomenon after entering the arc furnace when it

suddenly encounters heat, resulting in pressure fluctuations in furnace, which affects the safety of production [7,8].

The studies on the heating of pellets mainly focus on the pellet composition ratio and roasting process [9,10,11], and there is a lack of research on the preheating and drying process of ferromanganese pellets and preheating equipment. Kashinath et al. [12] established the effect of ore mineralogy on the drying characteristics of the pellets by investigating the cold crushing strength (CCS), porosity, and morphology of the preheated pellets. Kant et al. [13] proposed optimization measures for preheating temperature by using acicular iron ore pellets. The use of microwaves as a heat source to study the drying process and roasting characteristics of iron ore pellets is also a commonly available option [14,15]. Although belonging to nonferrous metallurgy, Matyukhin et al. [16,17] based on production data, established the gas-dynamic process of the pellet shaft kiln in the production of nonferrous metals and proposed measures to improve it, which has become an important basis for the study of preheating and drying process of ferromanganese and ferrochrome. In addition, the heated drying experiments carried out on the moisture content of various particles and their drying with the background of non-metallic particles, such as solid particles of grains, wood and other raw materials, are also of great reference significance [18,19].

Since the pellet preheating and drying process is in a high temperature environment, experimental operation and measurement are difficult, Computational Fluid Dynamics (CFD) have been widely used. The earliest numerical simulation methods applied to the preheating of pellets are mainly centered on the changing process of individual particles, Amani et al. [20] proposed a one-dimensional model that can be integrated with the reactor scale model by solving the transient differential equations for single pellet, and Backman et al. [21,22] also established the preheating and drying mathematical model for single pellet and compared with experimental results. With the wide application of porous media model (PMM), Hong et al. [23] used a PMM for the parametric study of preheated drying of pellets. The PMM also enables the study of heat and mass transfer process, porosity, bed void fraction and consolidation process and the development of drying kinetic model (DKM) [24,25,26,27]. Li et al. [28] investigated the effect of the preheating temperature and time of pellets on their simulated gas-based direct reduction behavior in a shaft kiln. The use of numerical simulation methods is equally relevant for tail gas emission and waste heat utilization, Nordgren et al. [29] used simulation methods to accurately describe the process of preheating pellets using waste heat to achieve green production. The discrete element method (DEM) is one of the most important means to study the particle motion, so numerical methods based on CFD-DEM coupling have been applied to the study of pellet preheating in a large number of applications. Ljung et al. [30,31,32] firstly investigated the effect of humidity on the preheating of pellets by using the traditional CFD method and established a mathematical model of pellet drying based on the PMM for a single pellet, after that, coupled the DEM model for the study of the distribution of the particles in the furnace.

Low-grade thermal energy for raw material preheating is a promising energy utilization technology [33,34]. It is adapted to local conditions, supports a wider range of fuels, and also reduces emissions, which is one of the directions of development for cleaner production [35].

All of the studies provide references to study the preheating process of pellets and the effect of evaporation. However, there is no research on the preheating efficiency of pellets with different particle sizes. At the same time, there is a lack of research on the preheating and drying process of ferromanganese pellets using high-temperature tail gas. Especially after entering the 1990s, small and

lightweight preheating shaft kilns have been emphasized, while the research on this kiln type has progressed slowly, and the prospect of utilizing high-temperature tail gas from arc furnaces for pellet preheating and drying has been insufficiently assessed. Therefore, this study takes an operating arc furnace roof preheating kiln as the background, establishes a PMM and shrinking core model (SCM) for studying the effect of pellet preheating heating and drying, and compares it with the current production data to examine the utilization prospect of this type of equipment.

2. Mathematical models

Simulating the preheating problem in a preheating shaft kiln with a PMM is essentially adding a momentum loss source term to the momentum equation to calculate the pressure drop caused by the flue gas flow through the material gap.

It is common to use Ergun's equation to solve the problem with the following formula:

$$\frac{|\nabla p|}{L} = \frac{150\mu(1-\gamma)^2}{D_p^2\gamma^3}v_\infty + \frac{1.75\rho(1-\gamma)}{D_p\gamma^3}v_\infty^2 \tag{1}$$

The viscous resistance coefficient and inertial resistance coefficient are:

$$\frac{1}{\alpha} = \frac{150(1-\gamma)^2}{D_p^2\gamma^3} \ , \quad C_2 = \frac{3.5(1-\gamma)}{D_p\gamma^3} \tag{2}$$

For the dehydration and drying process of a single pellet, the SCM can be utilized for simulation calculation. The equations controlling the the pellets moisture in the kiln are:

$$\frac{\partial}{\partial t}\left((1-\phi)\rho_s C_i\right) + \nabla\cdot\left((1-\phi)V_{\text{grate}}\rho_s C_i\right) = -R_i \tag{3}$$

When the pellet average moisture is higher than the critical moisture, the drying rate is shown in equation (4). When the average moisture of the pellet is lower than the critical value, see equation (5). When the wet core temperature reaches 373 K see equation (6).

$$R_w = a_v Sh\frac{D_w}{d_{\text{pel}}}\left(W_g^e - W_g^\infty\right) \tag{4}$$

$$R_w = \frac{a_v\left(W_g^e - W_g^\infty\right)}{\dfrac{r_{\text{pel}}\left(r_{\text{pel}} - r_w\right)}{2r_w D_w^e} + \dfrac{1}{k_w}} \tag{5}$$

$$R_w = \frac{3k_p\left(P^e - P^{\text{atm}}\right)}{\dfrac{r_{\text{pel}}^3}{r_w} - r_{\text{pel}}^2} \tag{6}$$

$$D_w^e = D_w\frac{\varepsilon}{\tau} \ , \quad D_w = 1.2\times10^{-9}T_g^{1.75} \ , \quad \tau = \varepsilon^{-0.41} \ , \quad P^e = 133.3\exp\left(A - \frac{B}{C + T_s}\right) \tag{7}$$

where A = 18.3036, B = 3816.44 and C = - 46.13.

$$T_w = 173.4 - 4.166r_h + 2.57 \times 10^{-2} r_h + T_g(0.3648 + 1.4585 \times 10^{-2} r_h - 8.688 \times 10^{-5} r_h^2) \ \ T_s \leq 373 \ K \tag{8}$$

$$T_w = 197.7 + 125.753r_h - 11.64749r_h^2 + T_g(0.3964 - 0.697929r_h + 6.3175 \times 10^{-2} r_h^2)$$
$$+ T_g^2(-2.921 \times 10^{-4} + 9.86139 \times 10^{-4} r_h - 8.577 \times 10^{-5} r_h^2) \ \ T_s \geq 373 \ K \tag{9}$$

The gas energy equation:

$$\frac{\partial}{\partial t}\left(\gamma \rho_g c_{pg} T_g\right) + \nabla\left(\gamma \vec{v} \rho_g c_{pg} T_g\right) = \nabla \cdot \left(k_g \nabla T_g\right) - a_v h_v\left(T_g - T_0\right) \tag{10}$$

The pellet energy equation:

$$\frac{\partial}{\partial t}\left((1-\gamma)\rho_o c_{po} T_o\right) + \nabla \cdot \left(\vec{v}_{down}(1-\gamma)\rho_o c_{po} T_o\right) = \nabla \cdot \left(\left(k_0 + e_b\right)\nabla T_o\right) + a_v h_v\left(T_g - T_o\right) \tag{11}$$

The radiation between the pellets is calculated as:

$$e_b = 16\sigma T_o^3 / (3\beta) \tag{12}$$

The convective heat transfer coefficient of the pellet can be calculated as:

$$h_v = \frac{Nu \cdot \lambda_g}{l_z} \tag{13}$$

$$Nu = Pr^{1/3} \cdot \frac{1.6274 Re^{-0.575}}{\gamma} \ , \ l_z = 0.0178\rho^{0.596} \tag{14}$$

$$Re = \frac{\rho_g \cdot D_p \cdot u}{\mu} \ , \ Pr = v / a \tag{15}$$

$$a = \frac{\lambda_g}{\rho_g c_{pg}} \tag{16}$$

The equation for solving the specific surface area during gas-solid convection heat transfer in a preheating shaft kiln is as follows:

$$a_v = (1-\gamma) \times \frac{S_p}{V_p} \tag{17}$$

Heat radiated from flue gas to pellets using the P-1 model:

$$-\nabla q_r = aG - 4a\sigma T^4 \tag{18}$$

3. Physical model

3.1. Geometric modeling and operating principles

In this paper, the preheating shaft kiln is used as part of the smelting system of an arc furnace

4

for ferromanganese in a plant. The main equipment components in this system are shown in Figure 1. The preheating shaft kiln is an approximate annular structure, with a maximum diameter of 9.18 m. The inner side is the chamber where the high-temperature flue gas stays, with a diameter of 5.33 m. Between the inner side and the outer side is the workspace in which the pellets are preheated, and the storage, preheating, and cooling segments are respectively located from top to bottom. The maximum width of the preheating section is 1.925 m, and the narrowest width at the closure below the preheating section is 0.95 m. The maximum and narrowest widths of the cooling section are the same as those of the preheating section. After entering the preheating shaft kiln, the ferromanganese pellets quickly pass through the storage segment and enter into the preheating segment, so it can be assumed that there is no retention of the pellets in the storage segment, i.e., there is no accumulation. The pellets move downward in the preheating segment with time. At the same time, the blower sends the high temperature flue gas into the flue gas chamber of the preheating shaft kiln. The high temperature flue gas from the gas chamber enters the preheating segment from the flue gas inlet and makes a heat and mass transfer with the ferromanganese pellets. Under the action of high-temperature flue gas, the temperature of ferromanganese pellet gradually increases and the water content gradually decreases, and finally it is discharged from the preheating shaft kiln through the cooling segment and pellet outlet, and enters into the transportation pipe, and finally enters into the arc furnace (Figure 2).
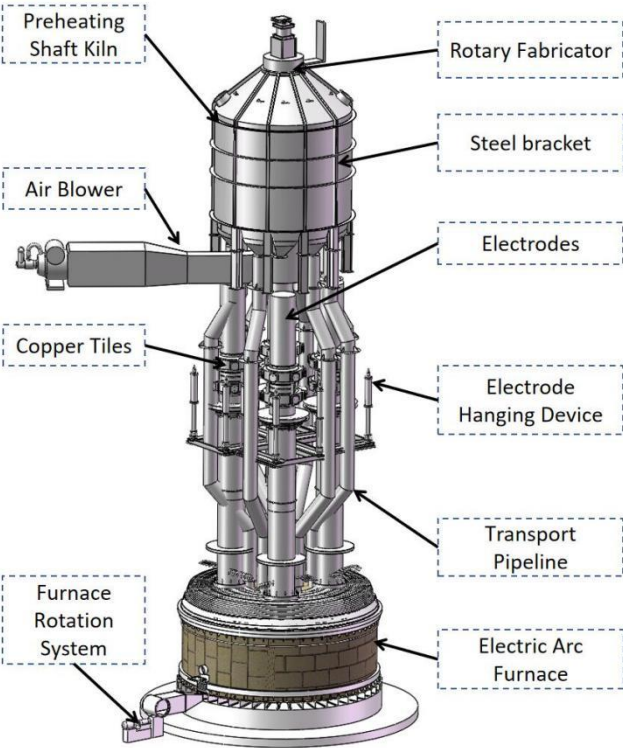

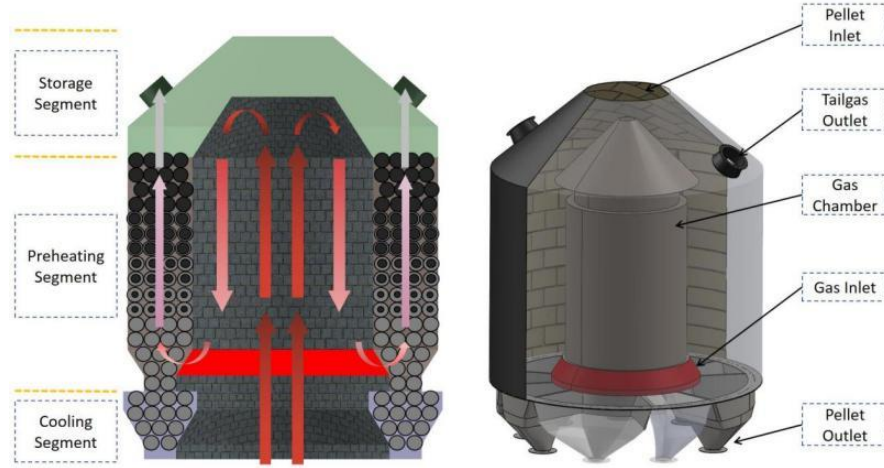**Figure 1. Schematic diagram of the composition of the Submerged Arc Furnace**

Figure 2. Composition and operation principle of preheating shaft kiln

3.2. Boundary conditions and solution methods

In this paper, a three-dimensional model was established in 1:1 according to the real size, and the external structures, such as the steel structure and fabricator, which do not affect the calculation, were neglected, while the wall was regarded as an adiabatic boundary without heat-mass transfer with the outside, and the inside was regarded as the fluid domain. The storage segment is the gas region, while the preheating and cooling segments are the porous media region.

In the pelleting process of ferromanganese, the diameters are generally considered to be most suitable between 6 mm~16 mm, so 11 sizes of this interval value are used in this paper for the study. Other solution conditions are summarized in Table 1.

Table 1. Calculation conditions and values

Calculation conditions	Values
Flue gas inlet velocity/(m·s^{-1})	3
Flue gas inlet area/(m^2)	16.5
Flue gas initial temperature/(K)	993
Tail gas outlet area/(m^2)	0.65468 × 2
Pellet entrance area/(m^2)	6.8349
Initial pellet temperature/(K)	300
Pellet initial humidity/(kg·kg^{-1})	0.007822
Velocity of pellet movement/(m·s^{-1})	0.0012111
Density/(kg·m^{-3})	2200
Thermal Conductivity/(W·m^{-1}·K^{-1})	0.296(300 ℃), 0.319(400 ℃), 0.335(500 ℃)
Specific heat capacity/(kJ·kg^{-1}·℃^{1})	1.22

Different ferromanganese pellet particle sizes filled into the preheating shaft kiln resulted in corresponding changes in the bed void ratio and the resulting viscous and inertial resistance, as shown

in Table 2.

In production, the gas inlet velocity cannot be measured directly. The preheating shaft kiln is embedded with a couple of sensors, which are converted by the control system to obtain the gas velocity. Currently this kiln is used in actual production with 10 mm pellets, and the gas inlet velocity is about 3 m/s.

Since the heat dissipation at the wall is neglected, the diffusion flux of the boundary condition of the energy equation at the wall position is set to zero. The pressure coupling is selected for calculation, and the semi-implicit (SIMPLE) method is utilized to solve the coupling problem of velocity and pressure; the k-equation and ε-equation in the turbulence equations are solved by the first-order upwind format, and the rest of the equations are processed by the second-order upwind format; in order to ensure the accuracy of the calculations, the convergence factor of the equations in this paper is set to 10^{-6}.

Table 2. Void fractions and resistances

Diameter/(mm)	Void fraction	Viscous resistance/(m^2)	Inertial resistance/(m^{-1})
6	0.36963	8132785.359	7281.329651
7	0.37023	5934790.752	6204.933791
8	0.37082	4513700.833	5398.380818
9	0.37141	3542758.215	4771.250567
10	0.372	2850643.074	4269.714816
11	0.37272	2336908.963	3854.683348
12	0.37344	1947837.451	3509.029029
13	0.37416	1646342.67	3216.739845
14	0.37488	1408141.435	2966.378664
15	0.3756	1216799.143	2749.558276
16	0.37632	1060874.828	2559.988291

4. Results and Discussion

4.1. Modelling validation

The preheating shaft kiln is meshed in the fluid domain using the Polyhedra method, resulting in three different numbers of meshes (N1 = 30,000, N2 = 60,000 and N3 = 100,000). The method generates meshes from the geometric surface towards the center, which can significantly reduce the number of meshes while ensuring the quality of the meshes compared to the traditional methods such as Tetrahedral and Hexcore. The temperature variations of the preheating segments under three meshes are analyzed and discussed. The temperature of the N1 mesh is not consistent with that of the N2 and N3 meshes, while the temperature of the N2 and N3 meshes are closer to each other, with an error of less than 5% between them. The results show that the number of N2 grids already meets the

calculation accuracy requirements, and further increasing its grid number to N3 does not have a significant effect on the results, so the N2 grid is finally adopted.
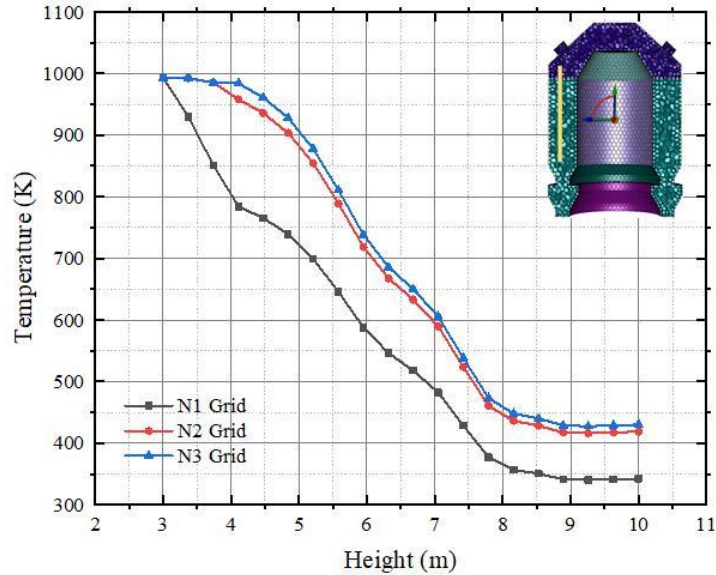

Figure 3. Grid-independent validation of gas temperature in a preheating shaft kiln

Since in the current production 10 mm pellets are used and the high temperature flue gas enters the preheating segment at a speed of about 3 m/s or so, the simulation results are compared with the field measurements according to this condition.

The temperature change of the tail gas of the preheating shaft kiln was measured by two sets of temperature sensors set at the tail gas outlet, and the temperature data were transmitted to the control console in real time. By comparing the simulated and measured gas temperatures at the two tail gas outlets (Figure. 4), the errors were 1.3% and 2% respectively, indicating that the simulation results were in good agreement.
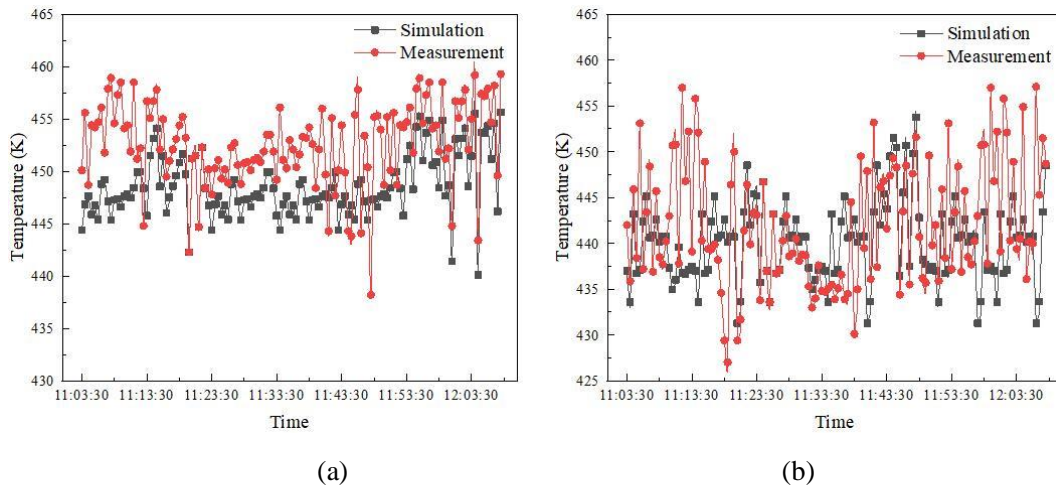

(a)   (b)

Figure 4. Comparison of tail gas temperature simulation and measure results: (a)-Outlet1; (b)-Outlet2

4.2. Gas temperature field

The gas temperature field in the lower part of the preheating segment shows large differences for the three particle sizes. Among them, 6mm particle size forms a large high-temperature zone, and the gas temperature reached more than 995 K (Figure 5a), while 10 mm and 16 mm did not form a high-temperature zone, and the temperature of the preheating segment is more uniform (Figure 5b, c). The gas temperature distribution in the storage segment is basically the same for the three particle sizes, and the tail gas is not discharged from pellet inlet.
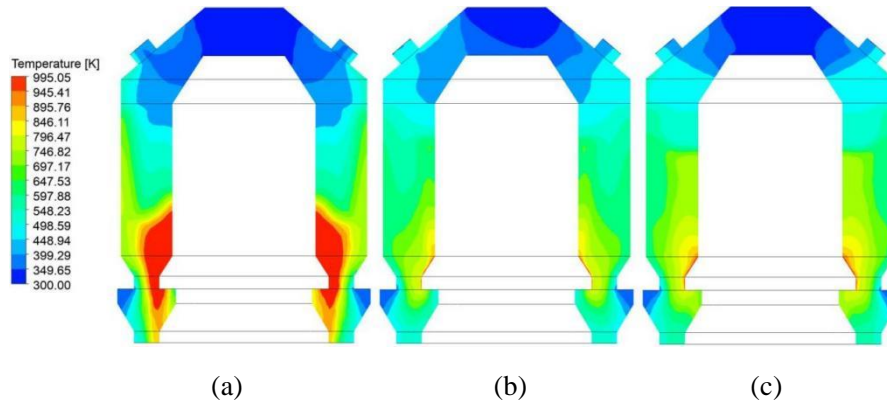

(a)   (b)   (c)

Figure 5. Comparison of gas temperatures at three particle sizes (a)-6mm; (b)-10mm; (c)-16mm

The gas temperatures in the middle and upper part of the preheating segment are analyzed with time using the heights of 6 m and 8.5 m as the objects, respectively. At H = 6 m, the gas temperature rises significantly after 800 s for pellet size of 6 mm~8 mm, while the pellet size of 9 mm~16 mm is significantly warmed after 400 s. At 1100 s, the gas temperature tends to stabilize and no longer undergoes a large change, and it shows the characteristic that the gas temperature is higher than that of small particle size under large particle size (Figure 6a). At H = 8.5 m, the gas heating under each particle size is slower, and after the gas temperature tends to stabilize, the gas temperature in the bed of large particle size is higher than that in the bed of small particle size more obviously (Figure 6b). The results of the gas temperature change in the preheating segment show that there is a hysteresis in the gas warming in the small-size bed. The gas heating rate is different for each particle size, however, the final gas temperature difference in the preheating segment is small.
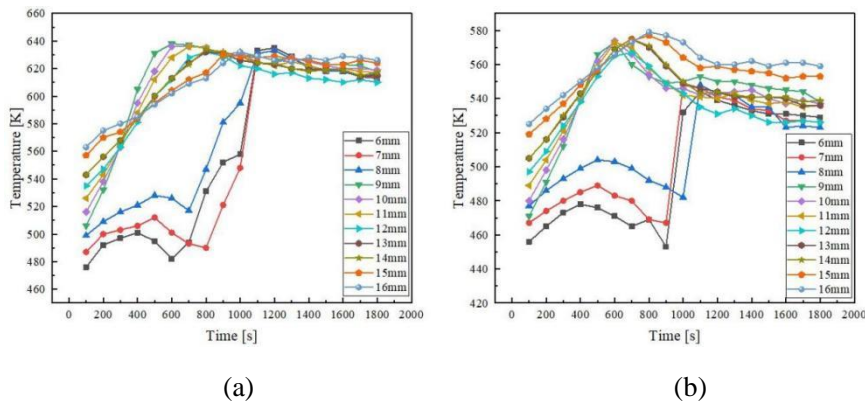

(a)   (b)

Figure 6. Unsteady state trends in gas temperature: (a)-H=6m; (b)-H=8.5m

4.3. Pellet temperature field

The temperature of the pellets after preheating is an important index to judge the preheating effect. Due to the smaller void ratio, 6 mm pellets formed a high temperature zone above 800 K in the lower part of the preheating segment (Figure 7a), and the temperature of the pellets in the middle and the upper part of the pellet was maintained at 450 K~650 K, and the overall preheating effect was better. When the pellet increases to 10 mm and 16 mm (Figure 7b, c), the high temperature zone shrinks, and the temperature of the cooling zone is maintained at about 600 K. Due to the increased void ratio, the gas can pass through the bed more easily, and the temperature of 10 mm and 16 mm pellets is obviously higher than that of 6 mm, which is consistent with the results of the gas temperature distribution.
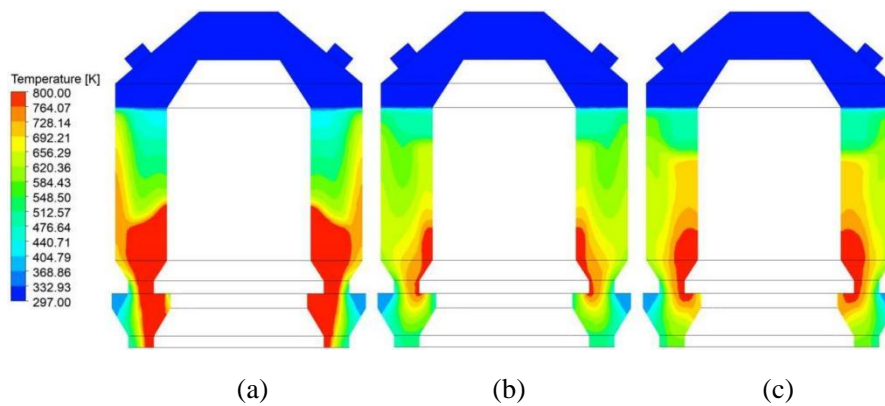

(a)   (b)   (c)

Figure 7. Comparison of pellet temperature at three particle sizes (a)-6mm; (b)-10mm; (c)-16mm

The final preheating temperature of the pellets is shown in Figure 8. When 6 mm~8 mm pellets reach the highest temperature at 1000 s after preheating, and stabilize thereafter. 9 mm~16 mm pellets reach the highest temperature at about 400 s, and stabilize with the preheating time. 1100 s later, the temperature of the pellets of various particle sizes basically remains unchanged. According to the result of the temperature at the outlet of the pellet, the preheating time can be shortened to 1100 s to realize higher preheating efficiency.
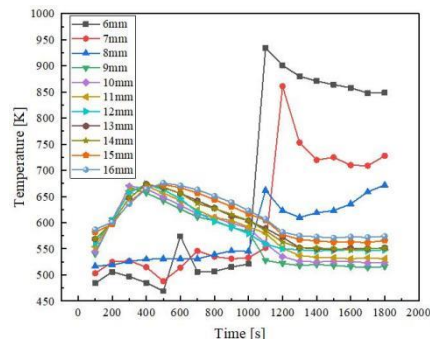

Figure 8. Variation of pellet outlet temperature for different particle sizes

4.4. Pellet moisture content

The moisture content of the pellets after preheating is another important index to judge the preheating effect. 6 mm and 10 mm pellets after preheating (Figure 9a, b), the preheating segment

below the middle of the pellet basically realized complete dehydration, the remaining moisture content is less than 0.001 kg/kg, and the moisture content at the upper part of the preheating segment close to the storage segment is less than 0.007 kg/kg. Although the temperature of the pellet was much higher than 373 K and the water evaporation process has already started, there is still a large amount of water inside the pellet due to the limitation of the reaction rate. This distribution indicates the high practical value of the shrinking core model applied to the preheating and drying of pellets, especially the process of moisture content change inside the pellet. In addition, the preheating temperature of the 16 mm pellet was slightly lower, but its water evaporation effect was still considerable, and basically achieved complete drying (Figure 9c).
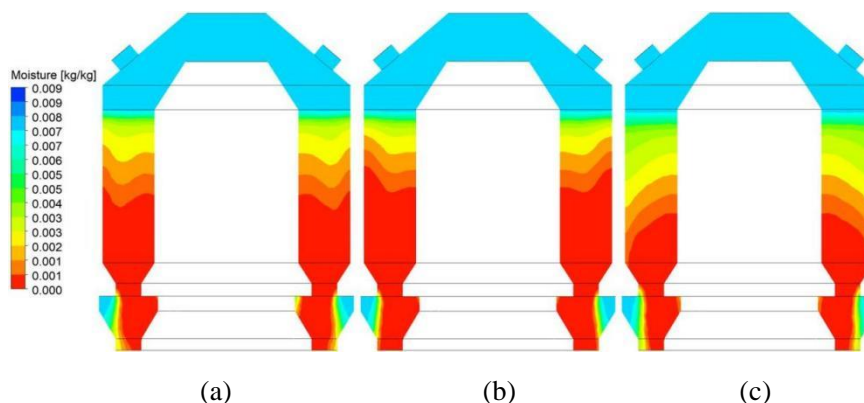

(a)   (b)   (c)

Figure 9. Comparison of moisture content of pellets at three particle sizes: (a)-6mm; (b)-10mm; (c)-16mm

For heat and water evaporation of individual particle sizes, the smaller the particle size, the faster its internal core heats up and the more rapid the evaporation process. However, for moving bed equipment consisting of a large number of particles, the gas passage efficiency due to the void ratio between particles has an important influence on the change of moisture content of the pellet. As shown in Figure 10, large particle size pellets such as 15 mm and 16 mm reach a stable dry state in about 500 s, while 6 mm~8 mm pellets also reach a stable dry state after 500 s, and the dehydration efficiencies of the largest and smallest particle sizes are basically the same. On the contrary, the dehydration efficiency of intermediate sizes such as 9 mm~11 mm is the highest, and the dehydration is completed in about 300 s, and the reaction time is obviously shortened. The dehydration time of each particle size indicates that the dehydration process of pellet is affected by both particle size and void ratio, while in the simulation results using only the PMM, the effect of void ratio on the heat and mass exchange process is often only shown.
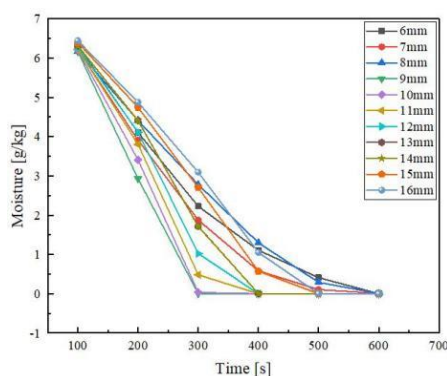

Figure 10. Variation of pellet outlet moisture for different particle sizes

11

5. Conclusions

As an important process before smelting in arc furnace, preheating and drying of pellets play an important role in ensuring production safety and reducing smelting power consumption. In this study, a mathematical model coupling PMM and SCM is established to reproduce the process of heating and drying of pellets inside the preheating shaft kiln.

Judging from the gas temperature field and the pellet temperature field, although the particle size of 6 mm~8 mm pellets is smaller, the temperature rises slowly because of dense bed. 8 mm pellets are the turning point of the heating rate, and the heating rate of the pellets larger than 8 mm increases significantly, and the heating time is shortened by about 200 s. Results show that the pellet temperature is basically stable after 1100 s, and the preheating time can be shortened to reduce the consumption of heat source and improve the production efficiency. The temperature at the pellets outlet also shows that the preheating effect of 6 mm~8 mm is the best, and the final temperatures of 9 mm and larger pellets are significantly lower than that of 6 mm~8 mm. The final temperatures of the pellets are not only affected by the particle size, but also by void ratios.

Although the final moisture content of the pellets of all particle sizes is lower than 0.001 kg/kg, the final completion of the dehydration time is affected by both the void ratio and the particle sizes. 9 mm~11 mm pellets basically completed the dehydration in about 300 s, with the highest dehydration efficiency. On the contrary, the dehydration time of 6 mm~8 mm pellets is up to 600 s, which reflects the double influence of particle size and void ratio on the dehydration rate.

Nomenclature

C	- linear anisotropic phase function coefficients	T_g	- gas temperature, [K]
C_2	- inertial resistance coefficient	u	- gas velocity, [m/s]
C_{p0}	- specific heat capacity of pellet, [kJ kg^{-1} K^{-1}]	*Greek symbols*	
C_{pg}	- gas specific heat capacity, [kJ kg^{-1} K^{-1}]	α	- thermal diffusion coefficient
D_p	- pellet diameter, [mm]	$1/\alpha$	- viscous resistance coefficient
D_w^e	- water diffusion coefficient	a_r	- absorption coefficient
G	- incident radiation, [W/m^2]	α_v	- specific surface area of pellet, [m^2]
h_V	- gas-solid convection heat transfer coefficient, [W m^{-2} K^{-1}]	β	- radiation convergence coefficients for porous media
l_Z	- characteristic length, [m]	γ	- void ratio
Nu	- Nusselt number	μ	- gas dynamic viscosity, [Pa·s]
P^e	- vapor equilibrium pressure, [Pa]	v	- gas kinematic viscosity, [m^2/s]
Pr	- Prandtl number	ρ_0	- pellet density, [kg/m^3]
Re	- Reynolds number	ρ_g	- gas density, [kg/m^3]
S_G	- radiative source term, [W/m^2]	σ	- Stephen Boltzmann's constant
T_0	- pellet temperature, [K]	σ_s	- scattering coefficient

References

[1] Olga, I. N., *et al.*, High-quality low-phosphorous manganese alloys for production of steel of low-temperature reliability, *Key Engineering Materials*, *839* (2020), 4, pp. 99-105

[2] He, B. B., *et al.*, High dislocation density-induced large ductility in deformed and partitioned steels, *Science*, *357* (2017), 8, pp. 1029-1032

[3] Gao, L., *et al.*, Upgrading of low-grade manganese ore based on reduction roasting and magnetic se Paration technique, *Science and Technology*, *54* (2019), 10, pp. 195-206

[4] Lowell, J., *et al.*, Electric arc furnaces to grow market share in US crude steel, *Inside Coal, & Steel Raw Materials*, *27* (2021), 09, pp. 1-4

[5] Lee, B., *et al.*, Effect of Hot Metal Utilization on the Steelmaking Process Parameters in the Electric Arc Furnace, *Steel Research International*, *86* (2014), 8, pp. 302-309

[6] Reynolds, C. S., *et al.*, Reducing Drying/Preheat Cycle Time to Increase Pellet Production at the BHP Whyalla Pellet Plant, *Ironmaking Conference Proceedings*, *56* (1997), pp. 343-358

[7] Feng, J. X., *et al.*, Drying and preheating processes of iron ore pellets in a traveling grate, *International Journal of Minerals, Metallurgy and Materials*, *017* (2010), 5, pp. 535-540

[8] Fan, X. H., *et al.*, Effect of carboxymethyl cellulose on the drying dynamics and thermal cracking performance of iron ore green pellets, *Powder Technology*, *267* (2014), 11, pp. 11-17

[9] Vieira, M. G., *et al.*, Effect of rheology and dispersion degree on the regrinding of an iron ore concentrate, *Journal of Materials Research and Technology*, *2* (2013), 10, pp. 332-339

[10] Huang, Z. C., *et al.*, Effect of wet-grinding of mix on quality of iron ore concentrate pellet, *Journal of Central South University of Technology (Natural science)*, *35* (2004), 6, pp. 753-758

[11] Tian, H., *et al.*, Utilization of ground sinter feed for oxidized pellet production and its effect on pellet consolidation and metallurgical properties, *Proceedings*, 11th International Symposium on High-Temperature Metallurgical Processing, San Diego, USA, 2020, Vol. 1, pp. 857-866

[12] Kashinath, B., *et al.*, Mineralogical investigation on preheating studies of high LOI iron ore pellet, *Powder Technology*, *418* (2023), pp. 2-12

[13] Kant, R. S., *et al.*, Optimization of Drying and Preheating Temperatures During Pellet Induration for Utilizing Goethitic Iron Ores, *Mining Metallurgy & Exploration*, *39* (2022), 4, pp. 43-44

[14] Lingyun, Y., *et al.*, Drying and roasting characteristics of iron ore pellets with microwave heating, *JOM*, *75* (2023), 6, pp. 3709 - 3717

[15] Covcevich, F. B. M., *et al.*, Iron ore pellet drying assisted by microwave: A kinetic evaluation, *Mineral Processing and Extractive Metallurgy Review*, *39* (2018), 4, pp. 266 - 275

[16] Matyukhin, V. I., *et al.*, Improvement of thermal modes of shaft furnaces of nonferrous metallurgy, *Russian Journal of Non-Ferrous Metals*, *51* (2010), 3, pp. 255-262

[17] Matyukhin, V. I., *et al.*, On modernization of air supply systems for improvement of gas distribution in shaft furnaces, *Solid State Phenomena*, *284* (2018), 10, pp. 1390-1397

[18] Huang, Y., *et al.*, Biofuel pellets made at low moisture content-influence of water in the binding

13

mechanism of densified biomass, *Biomass & Bioenergy*, *98* (2017), 3, pp. 1390-1397

[19] Gonzalez, J. F., *et al.*, Study of the influence of the composition of several biomass pellets on the drying process, *Biomass & Bioenergy*, *35* (2011), 10, pp. 4399-4406

[20] Amani, H., *et al.*, Mathematical modeling of thermal behavior of single iron ore pellet during heat hardening oxidation, *Journal of Thermal Analysis and Calorimetry*, *147* (2022), 2, pp. 2293-2303

[21] Ljung, A. L., *et al.*, Modelling the evaporation rate in an impingement jet dryer with multiple nozzles, *International Journal of Chemical Engineering*, *2017* (2017), pp. 1-9

[22] Tsukerman, T., Modeling and simulation of the drying kinetics of iron oxide pellets, M.Sc. thesis, Laval Universite, Quebec, Canada, 2006

[23] Hong, V. T., Influence of pore size distribution on drying behaviour of porous media by a continuous model, Ph.D. thesis, University of Magdeburg, Magdeburg, Germany, 2016

[24] José, T. F., *et al.*, On the influence of particles characteristics on moisture diffusivity during drying of granular porous media, *Advances in Chemical Engineering and Science, 04* (2014), 1, pp. 7-16

[25] Xiaohui, Fan., *et al.*, Effect of carboxymethyl cellulose on the drying dynamics and thermal cracking performance of iron ore green pellets, *Powder Technology*, *267* (2014), 11, pp. 11-17

[26] Sundarmurti, N. S., *et al.*, Effect of firing temperature and porosity on thermal conductivity and diffusivity of iron ore pellets, *ISIJ International*, *36* (2007), 8, pp. 991-999

[27] Tan, S., *et al.*, Modeling and simulation of iron ore pellet drying and induration process with accurate bed void fraction calculation, *Drying Technology*, *34* (2016), 6, pp. 651-664

[28] Li, W., *et al.*, Effects of preheating temperature and time of hongge vanadium titanomagnetite pellet on its gas-based direct reduction behavior with simulated shaft furnace gases, *Powder Technology*, *343* (2019), 2, pp. 194-203

[29] Nordgren, S., *et al.*, Effective use of available heat for maintaining a high green pellet temperature, *ISIJ International*, *53* (2013), 12, pp. 2072-2079

[30] Ljung, A. L., *et al.*, Convective drying of an individual iron ore pellet - Analysis with CFD, *International Journal of Heat & Mass Transfer*, *54* (2011), 17, pp. 3882-3890

[31] Ljung, A. L., *et al.*, Influence of air humidity on drying of individual iron ore pellets, *Drying Technology*, *29* (2011), 9, pp. 1101-1111

[32] Ljung, A. L., *et al.*, Discrete and continuous modeling of heat and mass transport in drying of a bed of iron ore pellets, *Drying Technology*, *30* (2012), 7, pp. 760-773

[33] Nikolova, L., *et al.*, Waste heat recovery at the glass industry with the intervention of batch and cullet preheating, *Thermal Science*, *20* (2016), 4, pp. 1245-1258

[34] Mohanasundaram, K., *et al.*, Effect of air preheating, exhaust gas recirculation and hydrogen enrichment on biodiesel/methane dual fuel engine, *Thermal Science*, *25* (2021), 1, pp. 449-464

[35] Filkoski, R. V., *et al.*, Energy optimisation of vertical shaft kiln operation in the process of dolomite calcination, *Thermal Science*, *22* (2018), 5, pp. 2123-2135